Resistance modeling of short-range connections: impact of current spreading

Davide Tierno[1]*, Victor Vega-Gonzalez[1], Simone Esposto[1,2], and Ivan Ciofi[1]

[1]*imec, Kapeldreef 75 – 3001 Leuven, Belgium*

[2]*Vrije Universiteit Brussel (VUB), 1050 Brussels, Belgium*

E-mail: davide.tierno@imec.be

We investigated the impact of current spreading on the resistance of short-range connections by performing simulations in Synopsys Sentaurus, based on a calibrated resistivity model. As a main case study, we considered Vertical-Horizontal-Vertical (VHV) connections, a novel cell routing architecture based on a two-level middle-of-line scheme, that has been proposed to boost the routing of 4-Track standard cells beyond the 2nm technology node. We analyzed the impact of vias and line geometry on VHV link resistance and we found that low aspect ratios (AR) lines are needed to minimize the average cell resistance. We performed extensive resistance simulations of various short-range connections schemes, beyond VHV links. We concluded that large AR lines are detrimental in all cases in which the link resistance is dominated by the vias. Finally, we show that ignoring current spreading can lead to a significant miscalculation of the link resistance in such scenarios.

1. Introduction

To ensure the continuation of Moore's law, it is critical to shrink the area of standard cells (SDC) by reducing both gate and metal pitches, which define SDC height and width, respectively [1, 2]. Although, due to fundamental physical limitations [3], it is becoming challenging to further reduce the height of each track (T), technology boosters such the fork-sheet device architecture [4, 5], Buried Power Rail [6, 7] and Self-Aligned Gate Contacts [8, 9] are expected to enable 5T SDC and eventually 4T SDC. Nonetheless, other challenges remain [10–13]. In fact, whereas in a 5T SDC a classical Horizontal Vertical Horizontal (HVH) routing approach could still be implemented, beyond that (*i.e.,* for 4T SDC) such a scheme would leave a very small accessibility window for input and output pins, as visible in Fig. 1a. In fact, in a standard HVH approach, the first back-end-of-line (BEOL) metal levels are along the horizontal (Mint), Vertical (M1) and Horizontal (M2) direction, respectively, with M2 being the first metal level used for place and route. The solution proposed to augment pin accessibility relies on implementing a Vertical-Horizontal-Vertical routing scheme [14-16], hence by accessing the pins along the horizontal direction (Fig.1b), *i.e.,* along the side of the SDC that has a larger aperture. This is achieved by introducing an additional vertical middle-of-line MOL layer (M0B in Fig. 1c) that is used for intra-cell routing, hence absorbing the BEOL M1 layers in the MOL. Eventually, M1 becomes the first metal level available for place and route, making more than 4 pins available for inter-cell routing in a 4T SDC. The intra-cell routing is realized by additional vias, V0A and VintB that are used to connect M0B to front-end-of-line (FEOL) devices and to Mint, respectively. Chehab et al. performed a block-level analysis of a 2-level 4T-VHV scheme and showed it can achieve a 21% higher Power-Performance-Area (PPA) compared to the traditional 5T-HVH FSH architecture [14]. Hence, VHV are a key scaling booster to enable 4T SDC for technology nodes beyond 2 nm [14-16]. In this work we first evaluate the impact of VHV link geometry, *i.e.,* the dimensions of V0A, M0B and VintB, on the VHV Link Resistance (R_{Link}) and SDC Resistance (R_{SDC}). As the SDC dimensions keep scaling, and metal lines become shorter, R_{Link} starts to be strongly impacted by current spreading (CS) [17]; the main consequence is that large AR lines do not always result in lower link resistance values. Eventually, in addition to [15], we performed an extensive study beyond the specific case of VHV links, highlighting the role of line CD and length on current spreading, providing a

general framework to optimize and properly evaluate the resistance of novel MOL and BEOL connection schemes, *e.g.,* hybrid heights schemes [18, 19].

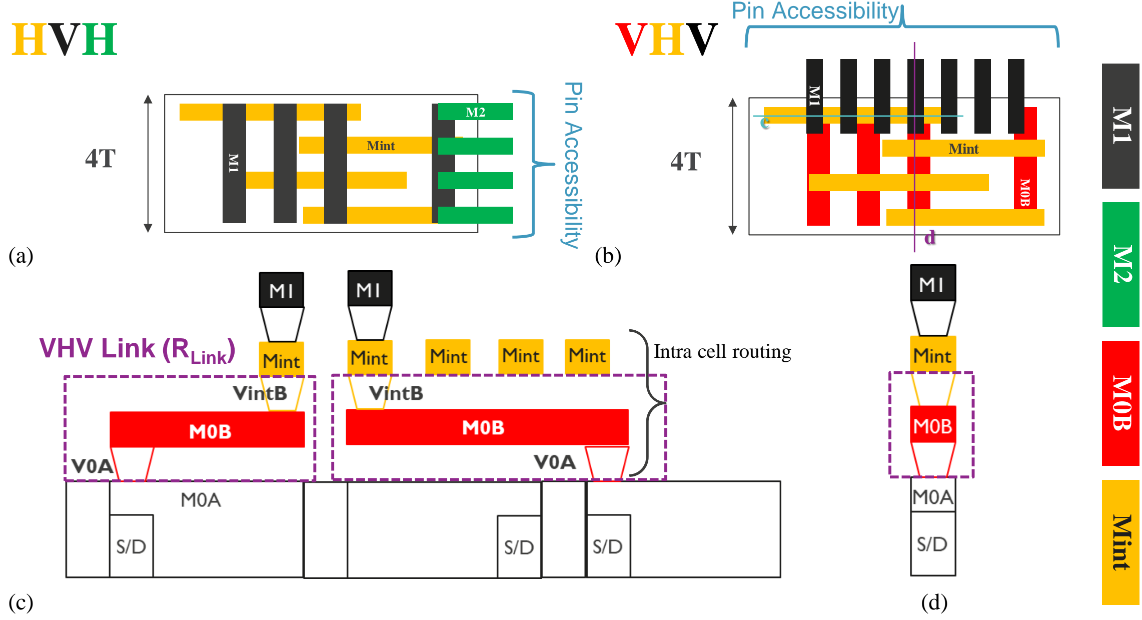

Fig. 1 Top view of a 4T SDC with (a) HVH and (b) VHV routing schemes. (c) and (d) Cross sections of a VHV link along the c and d lines drawn in (b) along Mint and M0B respectively.

2. Modelling of VHV links resistance

2.1 VHV model description

We generated a 3D model of an entire SDC with VHV links using Sentaurus Workbench® [20] (SWB) by implementing a semi-damascene integration flow (Fig. 2) [21-24]. A barrierless Ru metallization scheme was used for all the constituting elements of the VHV and Mint. The reliability of such an integration scheme for Ru has been experimentally demonstrated [25]. Potentially, other metallization schemes based on barrierless alternative metals can be used *instead of* or *in combination with* Ru [26]. In this study we focused on Ru only because the objective was to assess solely the impact of geometry on R_{Link} and R_{SDC}, as defined in Eq. (1) and Eq. (2), respectively:

$$R_{Link} = R_{V0A} + R_{M0B} + R_{VintB} \; (1)$$

$$R_{SDC} = \sum_{i=1}^{n} R^{i}_{Link} \; (2)$$

Hence, R_{Link} refers to the collective resistance of the three constituting elements (R_{V0A}, R_{M0B}, R_{VintB}) of the novel MOL connection scheme, as indicated also in Fig. 1c and Fig. 1d by means of a dashed line. Neither the resistance of the FEOL devices nor the contribution of Mint is evaluated. R_{SDC} is the sum of all the links within a standard cell. The critical dimensions (CD) of V0A (12nm), M0B (17nm) and VintB (8nm) are fixed and determined by gate and metal pitch assumptions representative for a 2nm logic technology node. The lengths of the M0B lines are also fixed: 80% are 18.5nm-, 15% are 50.5nm- and 5% are 178nm-long. The percentages refer to the occurrence of the three M0B lengths across all the SDCs in the design library used in [14].

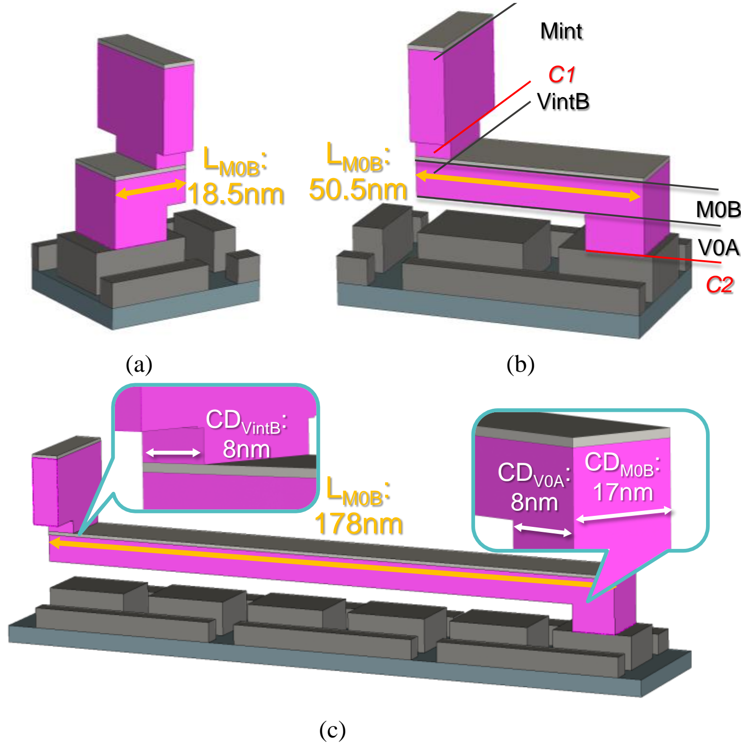

Fig. 2 SWB-generated 3D model of a VHV link (dielectric elements not shown) with links with (a) 18.5nm-long, (b) 50.5nm-long and (c) 178nm-long M0B lines. C1 and C2 indicate the positions of the contacts between which RLink was evaluated.

A complete overview of VHV dimensions is provided in Table I. As a consequence, the only free parameters that can be varied to optimize (*i.e.* minimize) R_{Link} are the heights of the two vias and (H_{V0A}, H_{VintB}) and of the line (H_{M0B}). For each M0B length, full 3D simulations were performed in Synopsys Sentaurus, using a calibrated resistivity model [17, 27, 28]. The model was calibrated using experimental Ru data [21, 24]. R_{link} was evaluated for a wide

range of H_{V0A}, H_{VintB} and H_{M0B} values, that are listed in Table I. A sensitivity analysis of the results with respect to mesh size was carried out to validate our settings for the simulations that are reported in the following section.

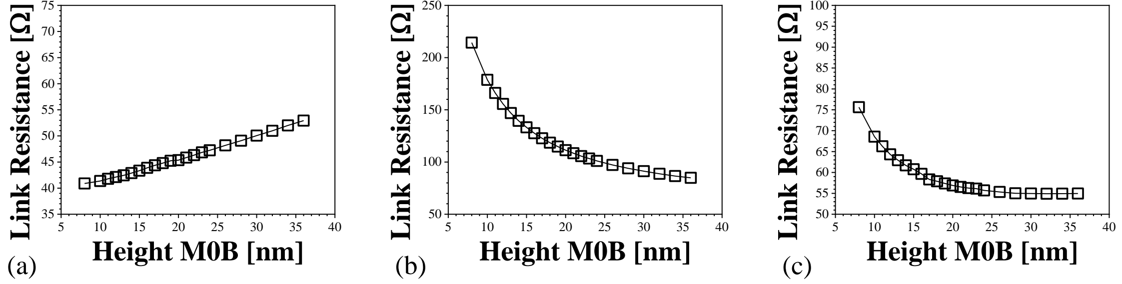

Fig. 3 Resistance of VHV Links with (a) 18.5nm-, (b) 50.5nm- and (c) 178nm-long M0B lines for various H_{M0B} values. For all the three cases, H_{VintB} and H_{V0A} were set to 4nm and 8nm, respectively.

2.2 Discussions of the simulation results

The link resistance (R_{Link}) for each of the three M0B lengths is shown in Fig. 3 as a function of M0B height, for a selected pair of V0A and VintB heights. Coherently with the definition of R_{Link} in Eq. (1), the contacts were placed at the interface between Mint and VintB (C1 in Fig. 2b) and at the interface between V0A and the FEOL (C2 in Fig. 2b). The analysis is limited to the smallest H_{V0A} and H_{VintB} values in order to emphasize the impact of H_{M0B}, and thus of the line AR, while minimizing the impact of the vias on R_{Link}. We observed a negative correlation between R_{Link} and H_{M0B} for 50.5nm- (Fig. 3b) and 178nm-lines (Fig. 3c) but, unexpectedly, a positive correlation for the 18.5nm-long lines (Fig. 3a). The different response obtained for the three lengths of M0B is better understood by analyzing the current density and potential distribution within the lines. The cross-sectional plots of the shortest and tallest 178nm-long M0B lines are shown in Fig. 4a and Fig.4b, respectively. In both cases, the current density is very uniform along the line length and the potential is uniformly distributed, indicating that the current flows mainly parallel to the line-length.

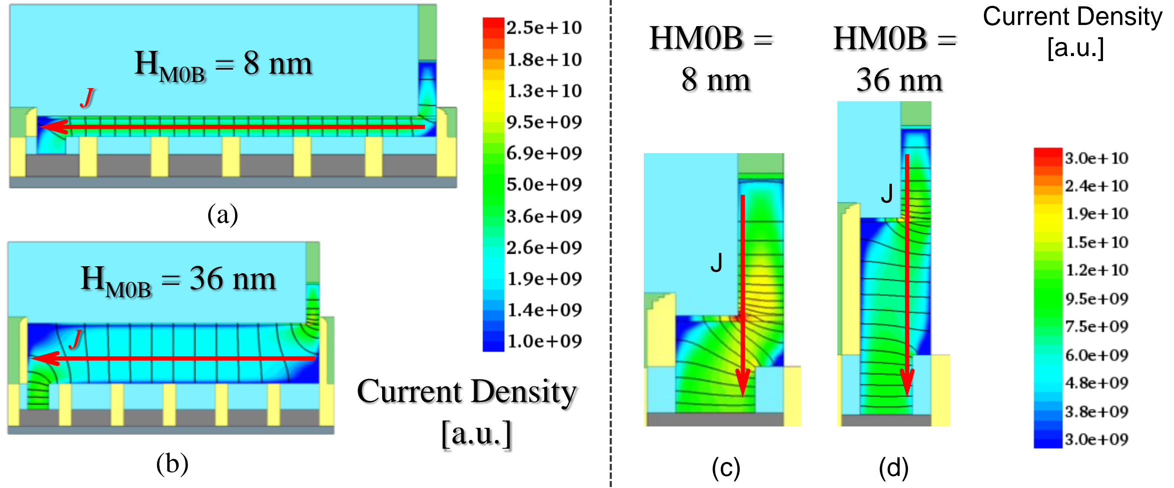

Fig. 4 Current density distribution within VHV Links with (a), (b) 18.5nm- and (c), (d) 178nm-long M0B lines. The black lines depict equipotential voltage values between the two ends of the VHV Link. The two extreme values for H_{M0B} are shown for the two M0B lengths, *i.e.* 8 nm in (a) and (c), 36 nm in (b) and (d). The red arrows clearly highlight the main direction of the current flow, *i.e.* parallel to M0B length in (a) and (b) and orthogonal to M0B length in (c) and (d).

A quite different response is instead observed for links with 18.5nm-long M0B lines, that are shown in Fig. 4c and Fig. 4d for H_{M0B} = 8 nm and H_{M0B} = 36nm, respectively. In fact, it can be seen that the current density as well as the voltage varies mainly along the height of the structure, *i.e.* orthogonal to the line length. Hence, by increasing the height of M0B the current path is also increased and so the link resistance. In these links, we clearly observed a large impact of current spreading [17], visible in a 10x increase in current density between the via-like conjunction points and the dead-end edges of the line (dark blue areas in Fig. 4c and Fig. 4d). To summarize, we observed two competing behaviors for the two (three) M0B line lengths, in VHV links with shorter M0B lines, R_{Link} is dominated by VintB and V0A resistances (R_{Vias}), with M0B behaving like a third via in between. Moreover, we observed a large current spreading effect, *i.e.* a not uniform current density at the via-line conjunction points. For links with longer M0B lines instead, line resistance becomes the dominant contribution to R_{Link}, hence benefiting from large H_{M0B} values, *i.e.* larger line AR. Finally, we explicitly investigated the impact of H_{V0A} and H_{VintB} on R_{Link}, as shown in Fig.5, by increasing the height of the two vias, R_{Link} increases for all line lengths. In links with 178nm-

long lines, M0B remains the major contribution to R_{Link} even for the largest H_{V0A} and H_{VintB} values, while the via-like behavior observed for systems with 18.5nm-long M0B lines, is enhanced by increasing the height of the two vias. It should be noted that VintB has a larger impact than V0A on R_{Link} due to the smaller dimensions of the former. Hence, we concluded that H_{V0A} and H_{VintB} should be maintained as short as possible to minimize R_{Link}.

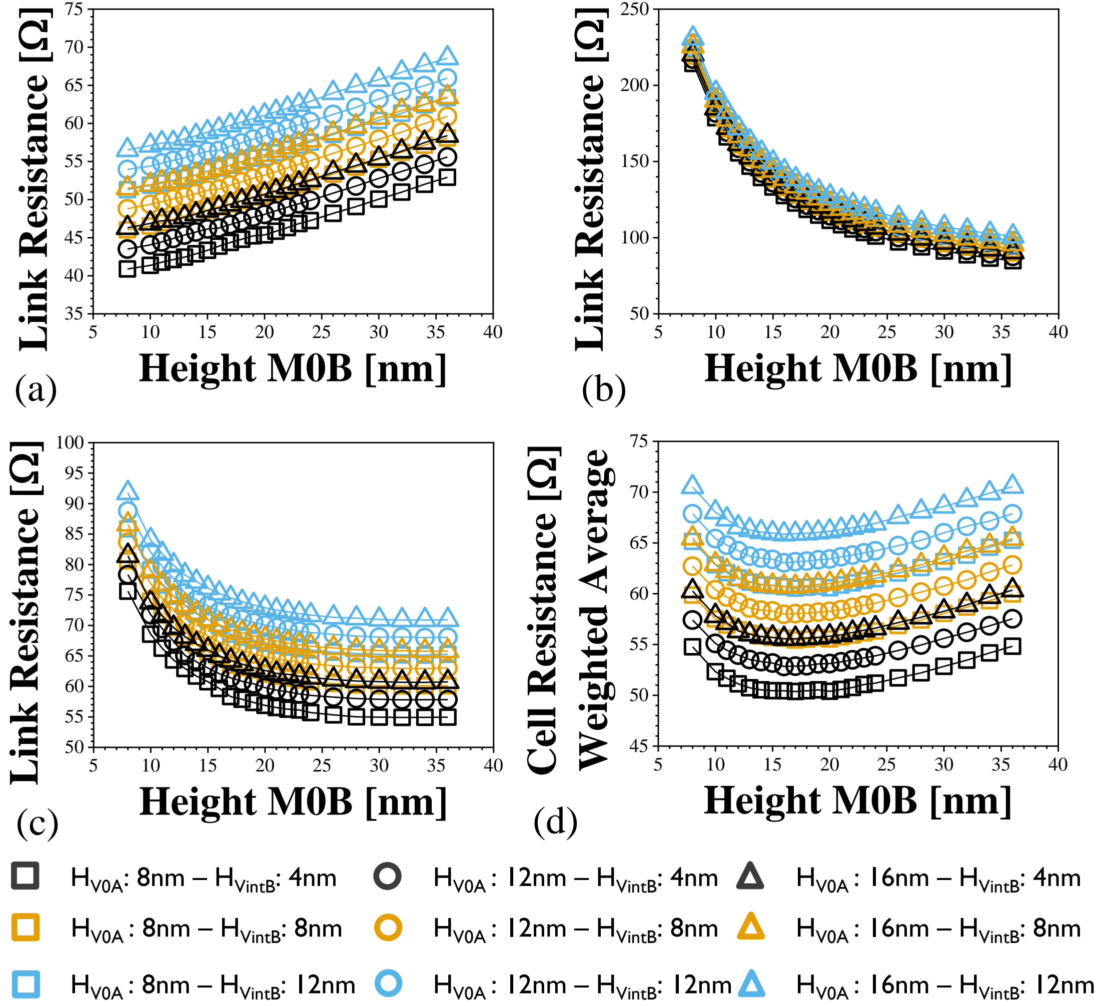

Fig. 5 Resistance of VHV Links with (a) 18.5nm-, (b) 50.5nm- and (c) 178nm- M0B lines. With respect Fig. 3, all H_{V0A} and H_{Vint} values listed in Table I are plotted. The variation of H_{V0A} and H_{Vint} does not alter the opposite behaviors observed for links with 18.5nm- and 178nm-long M0B lines. (d) Weighted Average Cell Resistance (R_{SDC}) based on Eq. (3).

2.2.1 Overall Cell Resistance Optimization

In order to find the optimal M0B height value that minimize the resistance value of the overall standard cell (R_{SDC}), we calculated the weighted cell resistance considering the line

lengths distribution across all SDCs:

$$R_{SDC} = 0.8 \cdot R_{link}^{18.5nm} + 0.15 \cdot R_{link}^{50.5nm} \cdot 0.05 \times R_{link}^{178nm} \quad (3)$$

As shown in Fig. 5d, R_{SDC} can be minimized for small H_{M0B} values, *i.e.* $H_{M0B} \in [12, 24]$ nm, and thus for low AR ($AR_{HM0B} \in [0.7, 1.4]$). Such unexpected outcome is caused by the overwhelming presence (80%) of links with 18.5nm-long M0B lines. It should also be noted that for different length distributions, different minima are observed.

3. Extensive study beyond VHV links

3.1 Description of the upgraded model

Eventually, we performed an extensive study by varying all the geometrical parameters of the via-line-via system, *i.e.* line and vias CD, line and vias height and line length in our Synopsys Sentaurus 3D model. The only simplification we made was to use the same CD for the line and the two vias in order to facilitate the assessment of their impact on the resistance of the link. The objective of upgrading the model was to better understand the impact of vias resistance and current spreading on short connections, as well as developing a framework that can be used beyond VHV links, *e.g.* for hybrid-height lines [18, 19]. The full set of dimensions is reported in Table II. The considered CDs are relevant for metal pitches ranging from 40 nm to 16 nm, *i.e.* for technology nodes down to A2 [30]. The extended study confirmed the substantial impact of R_{Vias} on R_{Link} when lines are shorter than 50nm. However, the outcome varies significantly depending on the CD of the line (and vias). In Fig. 6, the resistance values of links with various CDs and line lengths are plotted. For all CDs we observed the same two competing behaviors discussed above for VHV links: as the line length becomes shorter, large line AR are detrimental for the overall link resistance. In other words, whenever the line is “sufficiently short”, small AR should be preferred to minimize the link resistance.

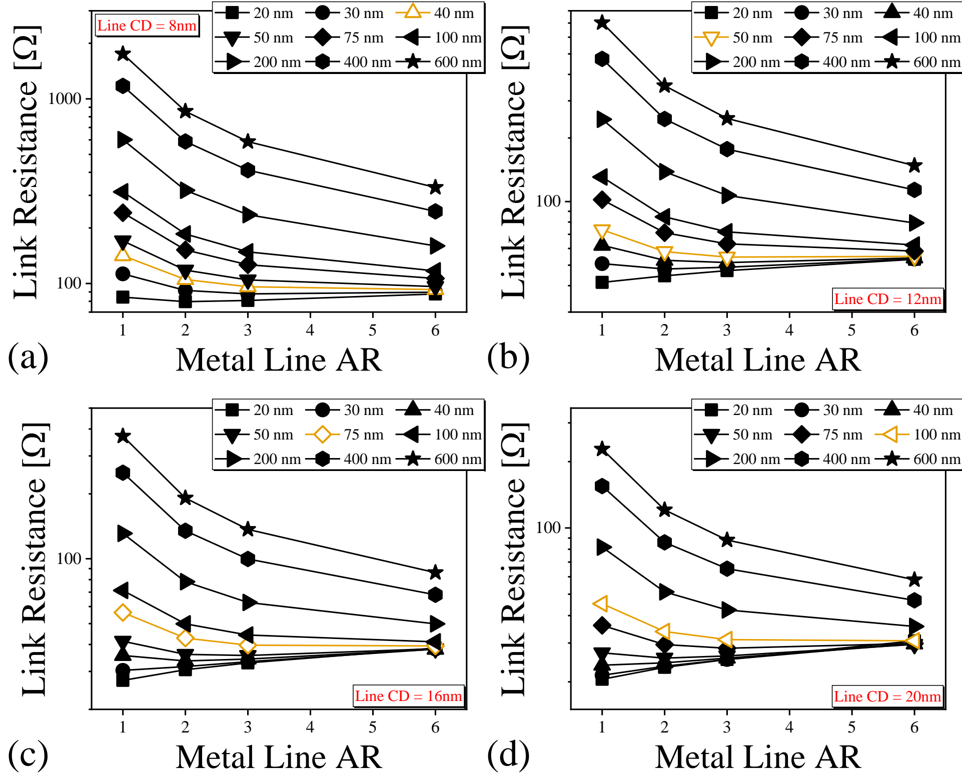

Fig. 6 Resistance of via-line-via links with (a) CD = 8 nm, (b) CD = 12 nm, (c) CD = 14 nm and (d) CD = 20 nm against the line AR. For all CDs, the two competing behaviors discussed in Fig. 3 for VHV links are visible. The orange empty symbols indicate the line length for which the resistance of the line becomes dominant over R_{Vias} and an increase in AR becomes beneficial for the overall link resistance.

As discussed above, we attribute the via-like behavior of short lines to the fact that current flows mainly orthogonal to the line length due to current spreading at the via-line junction points. Interestingly, we noticed that for the smaller CDs the via-like behavior appears to be negligible for very short lines (see Fig. 6a). Such a difference can be explained with the large increase in metal resistivity as feature sizes decrease [27, 29]. In fact, the smaller the line CD, the larger the line resistance (for a given length), the larger its impact on the link resistance. On the contrary, as the line contribution decreases the direct impact of vias on link resistance becomes dominant. For example, 20nm-CD lines exhibit the via-like behavior for all the simulated lengths up to 100 nm (Fig. 6d). Finally, it should be noted that the trends we observed, although studied for a wide range of CDs and lengths, are valid for the systems with a VHV-like configuration, *i.e.* with the two vias at opposite sides *and* at opposite ends

of the metal line. We expect the magnitude of the effect to be larger if the vias were to be on the same side of the metal line [31].

3.2 Sizing the effect of current spreading

All the cases considered and discussed so far show that, when dealing with a routing scheme based on a (short) line in between two vias, the overall link resistance does not correspond to the arithmetic sum of the resistances of the individual components, taken separately. In such systems, the current flows orthogonal to the line length rather than along it, mainly due to current spreading (see Fig. 4). Moreover, the current density within the line is quite not uniform and not the entire volume of the metal lines is fully used, resulting in a twisted current path that is difficult to predict *a priori*. Consequently, the effective resistance differs from the nominal one, given by the arithmetic sum of the resistances of the individual components. Based on the simulations performed in the extensive studied, we quantified the difference between the nominal and the effective (R_{Link}) resistance for the line-via-line system. The nominal resistance ($R_{Nominal}$) is defined as follows:

$$R_{Nominal} = R_{line} + R_{via}^{bottom} + R_{via}^{top} \quad (4)$$

where R_{line}, R_{via}^{bottom} and R_{via}^{top} are the resistance values for the line, top and bottom vias, respectively, obtained by simulating the resistance of the individual elements. In Fig. 7a, we plotted the ratio between the two values ($R_{Link}/R_{Nominal}$) for the entire data set. We observed (again) a large impact of line AR and line length on $R_{Link}/R_{Nominal}$, resulting in the overestimation or underestimation of the link resistance. On the one hand, we observed that R_{Link} is larger than $R_{Nominal}$ for shorter-, large AR-lines; for example, for systems with a 20nm-long line and AR 6, R_{Link} is 30% larger *on average* than the expected $R_{Nominal}$. Such an underestimation of R_{Link} may have a significant impact on system performances. On the other hand, AR 1 lines result in R_{Link} values smaller $R_{Nominal}$ for similar lengths. As expected, the difference diminishes significantly for longer metal lines; the difference is ~5% for systems with 600nm-long lines and AR < 6. Interestingly, the smallest difference between R_{Link} and $R_{Nominal}$ is observed AR 2 lines. We expect the difference to become entirely negligible for lines longer than 1 μm ($0.99 < R_{Link}/R_{Nominal} < 1.01$) [31]. As discussed above, the impact of current spreading depends on the feature size as well, as visible by comparing

Fig. 7b and Fig. 7c, that show the analysis done for the smallest (8 nm) and largest (20 nm) simulated CD.

4. Conclusions

We performed an extensive study on various short-range connection schemes and concluded that, depending on the link length, large AR metal lines can be detrimental when the resistance is dominated by the vias. In fact, current spreading strongly impacts current flow at via-line conjunction points and hence the current path. The most noticeable effect is the via-like behavior observed for short lines. Consequently, the effective resistance differs from the nominal one, given by the arithmetic sum of the resistances of the individual components. In the simplified approach that is typically used, the current is simply assumed to flow along the via/line with a 90° turn when crossing from one element into the other but in reality, that is not the case. As the length of the metal line increases, the impact of current spreading diminishes and the $R_{Link}/R_{Nominal}$ ratio tends to 1, *i.e.* the two values coincide. Finally, we showed that neglecting this effect in such scenarios can lead to a significant miscalculation of the resistance of short-rage connections that may have an impact on system performances.

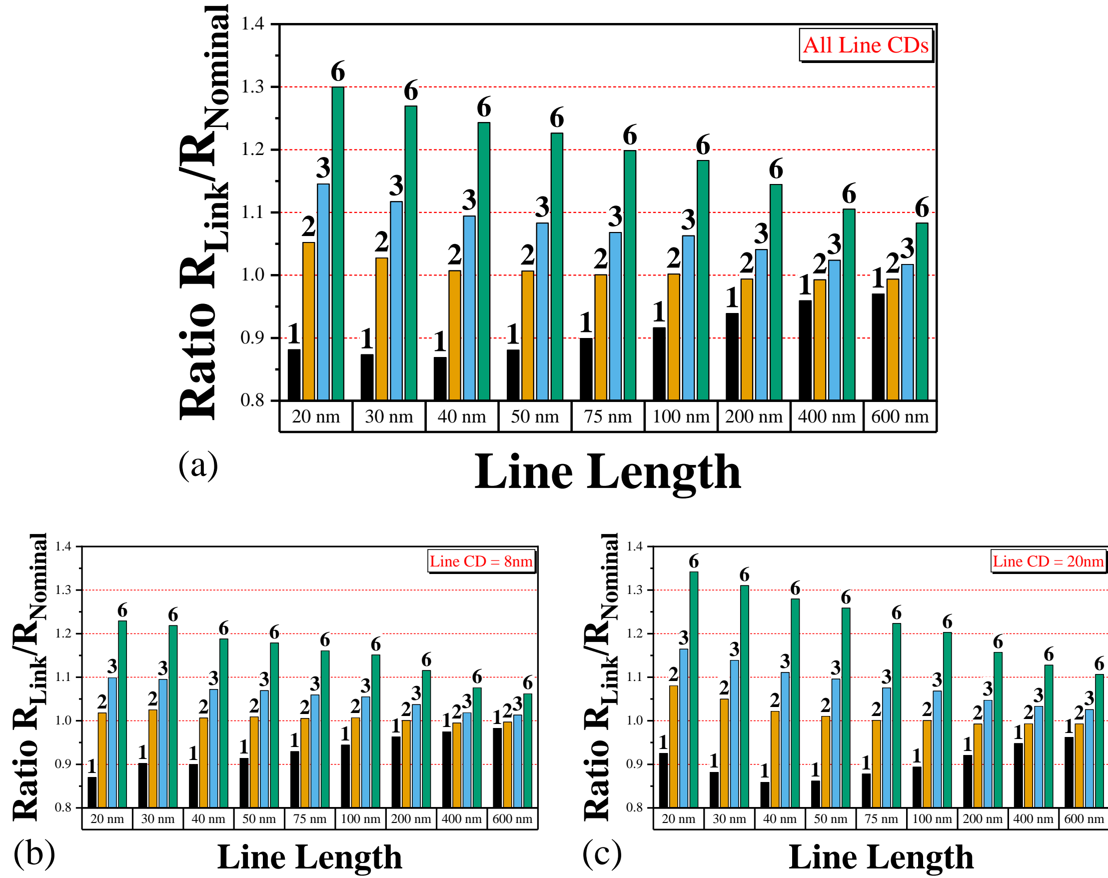

Fig. 7 Ratio between effective and nominal link resistance (see Eq. (4)) for various line lengths and line AR. The $R_{Link}/R_{Nominal}$ ratio quantifies the impact of current spreading on link resistance. The $R_{Link}/R_{Nominal}$ is shown for (a) the entire data set, (b) for systems with 8nm-wide features and (c) for systems with 20nm-wide features.

Acknowledgments

We would like to thank imec Nano IC and MOL programs for the support and the fruitful discussions.

References

1) L. Liebmann, J. Zeng, X. Zhu, L. Yuan, G. Bouche, J. Kye, In 2016 IEEE Symposium on VLSI Technology 2016 Jun 14 (pp. 1-2). IEEE.
2) S.B. Samavedam, J. Ryckaert, E. Beyne, K. Ronse, N. Horiguchi, Z. Tokei, I. Radu, M.G. Bardon, M.H. Na, A. Spessot, and S. Biesemans, In 2020 IEEE International Electron Devices Meeting (IEDM) (pp. 1-1). IEEE.
3) M.G. Bardon, Y. Sherazi, P. Schuddinck, D. Jang, D. Yakimets, P. Debacker, R. Baert, H. Mertens, M. Badaroglu, A. Mocuta, N. Horiguchi, D. Mocuta, P. Raghavan, J. Ryckaert, A. Spessot, D. Verkest, and A. Steegen, In 2016 IEEE International Electron Devices Meeting (IEDM) (pp. 28-2). IEEE.
4) P. Weckx, J. Ryckaert, V. Putcha, A. De Keersgieter, J. Boemmels, P. Schuddinck, D. Jang, D. Yakimets, M.G. Bardon, L.Å. Ragnarsson, P. Raghavan, R. R. Kim, A. Spessot, D. Verkest, and A. Mocuta, In 2017 IEEE International Electron Devices Meeting (IEDM) (pp. 20-5). IEEE.
5) P. Weckx, J. Ryckaert, E.D. Litta, D. Yakimets, P. Matagne, P. Schuddinck, D. Jang, B. Chehab, R. Baert, M. Gupta, Y. Oniki, L.Å. Ragnarsson, N. Horiguchi, A. Spessot, D. Verkest, In 2019 IEEE International Electron Devices Meeting (IEDM) (pp. 36-5). IEEE
6) A. Gupta, H. Mertens, Z. Tao, S. Demuynck, J. Bömmels, G. Arutchelvan, K. Devriendt, O.V. Pedreira, R. Ritzenthaler, S. Wang, D. Radisic, K. Kenis, L. Teugels, F. Sebaai, C. Lorant, N. Jourdan, B.T. Chan, H. Zahedmanesh, S. Subramanian, F. Schleicher, T. Hopf, A. Peter, N. Rassoul, H. Debruyn, I. Demonie, Y. Siew, T. Chiarella, B. Briggs, D. Zhou, E. Rosseel, A. De Keersgieter, E. Capogreco, E. Dentoni Litta, G. Boccardi, S. Baudot, G. Mannaert, N. Bontemps, A. Sepulveda, S. Mertens, M.S. Kim, E. Dupuy, K. Vndersmissen, S. Paolillo, D. Yakimets, B. Chehab, P. Favia, C. Drijbooms, J. Cousserier, M. Jaysankar, F. Lazzarino, P. Morin, E. Sanchez, J. Mitard, C. Wilson, F. Holsteyns, Zs. Tőkei, N. Horiguchi, In 2020 IEEE Symposium on VLSI Technology (pp. 1-2). IEEE.
7) A. Gupta, S. Kundu, L. Teugels, J. Bommels, C. Adelmann, N. Heylen, G. Jamieson, O.V. Pedreira, I. Ciofi, B. Chava, C.J. Wilson, and Zs. Tőkei, In 2018 IEEE International Interconnect Technology Conference (IITC) (pp. 4-6). IEEE.
8) D. Radisic, M. Demand, S. Chang, S. Demuynck, K. Kumar, A. Metz, L. Teugels, J. Sun, J. Smith, F. Sebaai, T. Hopf, and E. Altamirano, In Advanced Etch Technology for

Nanopatterning VIII (Vol. 10963, pp. 105-118). SPIE.
9) R. Xie, C. Park, R. Conti, R. Robison, H. Zhou, I. Saraf, A. Carr, S.S.C Fan, K. Ryan, M. Belyansky, S. Pancharatnam, A. Young, J. Wang, A. Greene, K. Cheng, J. Li, R. Conte, H. Tang, K. Choi, H. Amanapu, B. Peethala, R. Muthinti, M. Raymond, C. Prindle, Y. Liang, S. Tsai, V. Laminemi, A. Labonte, N. Cave, D. Gupta, V. Basker, N. Loubet, D. Guo, B. Haran, A. Knorr, and H. Bu, In 2019 Symposium on VLSI Technology (pp. T148-T149). IEEE.
10) J. Ryckaert, B. Chehab, D. Jang, G. Mirabelli, S.M. Salahuddin, P. Schuddinck, O. Zografos, A. Zubair, P. Weckx, and G. Hellings, In 2021 International Symposium on VLSI Technology, Systems and Applications (VLSI-TSA) (pp. 1-2). IEEE.
11) S.M.Y. Sherazi, Y.H. Chang, Y. Drissi, B. Chehab, J.U. Lee, V. Vega-Gonzales, and R.R.H. Kim, In DTCO and Computational Patterning (Vol. 12052, pp. 72-79). SPIE.
12) P. Schuddinck, O. Zografos, P. Weckx, P. Matagne, S. Sarkar, Y. Sherazi, R. Baert, D. Jang, D. Yakimets, A. Gupta, B. Parvais, J. Ryckaert, D. Verkest, and A. Mocuta, In 2019 Symposium on VLSI Technology (pp. T204-T205). IEEE.
13) G. Hellings, P. Schuddinck, S. Liu, S. Muhammad Salahuddin, G. Mirabelli, R. Chen, A. Veloso, A. Jourdain, G. Hiblot, N. Horiguchi, J. Ryckaert, In 2022 International Conference on Solid State Devices and Materials (G-10-01)
14) B. Chehab, O. Zografos, E.D. Litta, Z. Ahmed, P. Schuddinck, D. Jang, G. Hellings, A. Spessot, P. Weckx, and J. Ryckaert, In 2021 IEEE International Interconnect Technology Conference (IITC) (pp. 1-3). IEEE.
15) D. Tierno, V. Vega-Gonzalez, S. Esposto, I. Ciofi, In 2022 International Conference on Solid State Devices and Materials (G-2-04).
16) V. Vega-Gonzalez, D. Radisic, S. Choudhury, D. Tierno, A. Thiam, D. Batuk, G.T. Martinez, F. Seidel, S. Decoster, S. Kundu, D. Tsvetanova, A. Peter, H. de Coster, A. Sepulveda-Marquez, E. Altamirano-Sanchez, BT Chan, Y. Drissi, Y. Sherazi, J. Uk-Lee, I. Ciofi, G. Murdoch, N. Nagesh, G. Hellings, J. Ryckaert, S. Biesemans, E. Dentoni Litta, N. Horiguchi, S. Park, Zs. Tőkei, In 2022 IEEE International Electron Devices Meeting (IEDM). IEEE. (unpublished).
17) I. Ciofi, P.J. Roussel, Y. Saad, V. Moroz, C.Y. Hu, R. Baert, K. Croes, A. Contino, K. Vandersmissen, W. Gao, P. Matagne, M. Badaroglu, C.J. Wilson, D. Mocuta, and Zs.

Tőkei, IEEE transactions on Electron Devices, 64(5), pp.2306-2313.

18) R. Baert, I. Ciofi, S. Patli, O. Zografos, S. Sarkar, B. Chehab, D. Jang, A. Spessot, J. Ryckaert, and Z. Tőkei, In 2020 IEEE International Interconnect Technology Conference (IITC) (pp. 28-30). IEEE.
19) S. Paolillo, A. Moussa, G. Murdoch, F. Lazzarino, A.L. Charley, P. Leray, J. Hung, R. Koret, S. Wolfling, and A. Ger, In Metrology, Inspection, and Process Control for Microlithography XXXIV (Vol. 11325, pp. 206-212). SPIE.
20) G. Murdoch, Z. Tokei, S. Paolillo, O.V. Pedreira, K. Vanstreels, and C.J. Wilson, In 2020 IEEE International Interconnect Technology Conference (IITC) (pp. 4-6). IEEE.
21) G. Murdoch, M. O'Toole, G. Marti, A. Pokhrel, D. Tsvetanova, S. Decoster, S. Kundu, Y. Oniki, A. Thiam, Q.T. Le, O.V. Pedreira, A. Leśniewska, G. Martinez-Alanis, S. Park, and Z. Tokei, In 2022 IEEE Symposium on VLSI Technology and Circuits (VLSI Technology and Circuits) (pp. 1-2). IEEE.
22) A. Farokhnejad, S. Esposto, I. Ciofi, O. Zografos, P. Weckx, J. Ryckaert, P. Schuddinck, Y. Xiang, and Z. Tőkei, In 2022 IEEE International Interconnect Technology Conference (IITC) (pp. 136-138). IEEE.
23) https://www.synopsys.com/
24) A. Pokhrel, G. Marti, M. O'Toole, G. Murdoch, A. Gupta, S. Decoster, S. Kundu, E. Camerotto, Q.T. Le, A. Thiam, A. Lesniewska, S. Seongho and and Z. Tőkei, In 2022 IEEE International Interconnect Technology Conference (IITC) (pp. 61-63). IEEE.
25) A. Leśniewska, O.V. Pedreira, M. Lofrano, G. Murdoch, M. van der Veen, A. Dangol, N. Horiguchi, Z. Tőkei, and K. Croes, In 2021 IEEE International Reliability Physics Symposium (IRPS) (pp. 1-6). IEEE.
26) M. Hosseini, D. Tierno, J.W. Maes, C. Zhu, S. Datta, Y. Byun, M. Mousa, N. Jourdan, E.D. Litta, and N. Horiguchi, In 2022 IEEE International Interconnect Technology Conference (IITC) (pp. 145-147). IEEE
27) I. Ciofi, P.J. Roussel, R. Baert, A. Contino, A. Gupta, K. Croes, C.J. Wilson, D. Mocuta, and Z. Tőkei, IEEE Transactions on Electron Devices, 66(5), pp.2339-2345.
28) D. Gall, Journal of Applied Physics, 119(8), 2016, p.085101.
29) S. Dutta, K. Sankaran, K. Moors, G. Pourtois, S. Van Elshocht, J. Bömmels, W. Vandervorst, Zs. Tőkei, and C. Adelmann, Journal of Applied Physics, 122(2), 2017,

p.025107.
30) Imec, presented at Future Summits 2022, Antwerp (Belgium)17-18 May 2022
31) D. Tierno, in preparation for publication.

List of Figures

- **Fig. 1** Top view of a 4T SDC with (a) HVH and (b) VHV routing schemes. (c) and (d) Cross sections of a VHV link along the c and d lines drawn in (b) along Mint and M0B respectively.
- **Fig. 1** SWB-generated 3D model of a VHV link (dielectric elements not shown) with links with (a) 18.5nm-long, (b) 50.5nm-long and (c) 178nm-long M0B lines.
- **Fig. 3** Resistance of VHV Links with (a) 18.5nm-, (b) 50.5nm- and (c) 178nm-long M0B lines for various H_{M0B} values. For all the three cases, H_{Vint} and H_{V0A} were set to 4nm and 8nm, respectively.
- **Fig. 4** Current density distribution within VHV Links with (a), (b) 18.5nm- and (c), (d) 178nm-long M0B lines. The black lines depict equipotential voltage values between the two ends of the VHV Link. The two extreme values for H_{M0B} are shown for the two M0B lengths, i.e. 8 nm in (a) and (c), 36 nm in (b) and (d). The red arrows clearly highlight the main direction of the current flow, i.e. parallel to M0B length in (a) and (b) and orthogonal to M0B length in (c) and (d).
- **Fig. 5** Resistance of VHV Links with (a) 18.5nm-, (b) 50.5nm- and (c) 178nm- M0B lines. With respect Fig. 3, all H_{V0A} and H_{Vint} values listed in Table I are plotted. The variation of H_{V0A} and H_{Vint} does not alter the opposite behaviors observed for links with 18.5nm- and 178nm-long M0B lines. (d) Weighted Average Cell Resistance (RSDC) based on Eq. (3).
- **Fig. 6** Resistance of via-line-via links with (a) CD = 8 nm, (b) CD = 12 nm, (c) CD = 14 nm and (d) CD = 20 nm against the line AR. For all CDs, the two competing behaviors discussed in Fig. 3 for VHV links are visible. The orange empty symbols indicate the line length for which the resistance of the line becomes dominant over RVias and an increase in AR becomes beneficial for the overall link resistance.
- **Fig. 7** Ratio between effective and nominal link resistance (see Eq. (4)) for various line lengths and line AR. The $R_{Link}/R_{Nominal}$ ratio quantifies the impact of current spreading on link resistance. The $R_{Link}/R_{Nominal}$ is shown for (a) the entire data set, (b) for systems with 8nm-wide features and (c) for systems with 20nm-wide features.

Table I. Dimensions of the constituting elements of the VHV links

Element	CD [nm]	Simulated Height Values [nm]
V0A	12	8, 12, 16
VintB	8	4, 12, 16
M0B	17	8, 10, 11, 12, 13, 14, 15, 16, 17, 18, 19, 20, 21, 22, 23, 24, 26, 28, 30, 32, 34, 36

Table II. Dimensions of the constituting elements of the generic via-line-via links used for the extensive study.

Element	CD [nm]	Length	AR
Line	8, 10, 12, 14, 16, 18, 20	20, 30, 40, 50, 75, 100, 200, 400, 600	1, 2, 3, 6
Top Via	8, 10, 12, 14, 16, 18, 20		1, 2, 4
Bottom Via	8, 10, 12, 14, 16, 18, 20		1, 2, 4